JOURNAL OF GEOPHYSICAL RESEARCH, VOL. 104, NO. A6, PAGES 12,645–12,656, JUNE 1, 1999

Characteristics of mesospheric optical emissions produced by lightning discharges

Georgios Veronis, Victor P. Pasko, and Umran S. Inan

STAR Laboratory, Stanford University, Stanford, California

Abstract. A new two-dimensional cylindrically symmetric electromagnetic model of the lightning-ionosphere interaction includes effects of both the lightning radiated electromagnetic pulses (EMP) and the quasi-electrostatic (QE) fields, thus allowing effective studies of lightning-ionosphere interactions on time scales ranging from several microseconds to tens of milliseconds. The temporal and spatial evolution of the electric field, lower ionospheric electron density, and optical emissions calculated with the new model are used to investigate theoretically the effects of the lightning return stroke current waveform (i.e., the current rise and fall timescales) and of the observational geometry on the optical signals observed with a photometer. For typical lightning discharges of ~100 μs duration the ionospheric response is dominated by the EMP-induced heating leading to the highly transient and laterally expanding optical flashes known as elves. The optical signal characteristics are found to be highly sensitive to both the observational geometry and the current waveform. The onset delay with respect to the lightning discharge, the duration, and the peak magnitude of optical emissions are highly dependent on the elevation and azimuth angles of field of view of individual photometric pixels. The shape of the optical signal clearly reflects the source current waveform. For a waveshape with risetime of ~50 μs or longer a double-pulse shape of the photometric signal is observed. For cloud to ground lightning discharges of ~1 ms duration removing substantial amount of charge (i.e., ~100 C from 10 km altitude), heating and ionization changes induced by the QE field lead to the mesospheric luminous glows with lateral extent < 100 km, referred to as sprites.

1. Introduction

During the past few years, a dramatic new experimental evidence has demonstrated the electrodynamic coupling between electromagnetic fields produced by lightning discharges and the lower ionosphere. Phenomena indicating the lightning-ionosphere coupling include "early/fast" VLF events [e.g., *Inan et al.*, 1996a], sprites [e.g., *Sentman et al.*, 1995], blue jets [*Wescott et al.*, 1995], gamma ray bursts of terrestrial origin [*Fishman et al.*, 1994; *Inan et al.*, 1996b] and "elves" [*Fukunishi et al.*, 1996; *Inan et al.*, 1997].

The aforementioned experimental findings have been accompanied by a number of theoretical models. *Inan et al.* [1991] modeled the interaction of intense electromagnetic pulses (EMPs) released by lightning discharges with the lower ionosphere, assuming a Maxwellian dis-tribution function of ionosphere electrons heated by EMP. A one-dimensional (1-D) quasi-stationary fully kinetic model of ionization changes and exitation of optical emissions induced by heating of ambient electrons caused by lightning EMPs was developed by *Taranenko et al.* [1993a, b]. *Rowland et al.* [1995] developed a two-dimensional (2-D) model of the lightning EMP-ionosphere interaction assuming a fixed electron temperature (~6 eV) as a result of heating of the ambient electrons to saturation by the EMP.

The primary result of the EMP-ionosphere interaction is transient optical flashes now referred to as elves, documented with recent high time resolution photometric measurements [*Fukunishi et al.*, 1996]. Elves occur at ionospheric altitudes of > 80 km, have ~300 km lateral extent and endure for < 1 ms [*Inan et al.*, 1997]. The observed temporal and spatial aspects of elves are consistent with a 2-D modeling of the interaction with the lower ionosphere of EMPs, which indicated that elves would appear to expand laterally at a rate faster than the speed of light when observed from a distance [*Inan et al.*, 1996c, 1997].

The above mentioned models of lightning EMP ionosphere interaction have exclusively treated the "radiated" EMP pulse without accounting for the quasi-static (QE) field resulting from the sudden removal of charge in a lightning discharge. The separate treatment of the EMP is fully justified in most cases, since the charge removal and the establishment of a significant QE field is relatively slow (~1 ms), while the EMP

Paper number 1999JA900129.
0148-0227/99/1999JA900129$09.00

radiated by the return stroke is produced at the initial phase of the discharge and propagates through the system in less than 1 ms. The QE field, on the other hand, is the important driver for the luminous glows, referred to as sprites, typically occuring at 50 - 90 km altitudes with 10 - 50 km lateral extent and duration of a few to many tens of milliseconds [e.g., *Sentman et al.*, 1995; *Fukunishi et al.*, 1996; *Inan et al.*, 1997].

A quasi-electrostatic heating model, which leaves out the radiated EMP component, has been successfully applied to explain many aspects of sprites [e.g., *Pasko et al.*, 1997, and references therein], with the separate treatment of the QE field being fully justified in most cases due to the relatively slow development of the field and few milliseconds timescales of sprites. A new model of lightning-ionosphere interaction which includes the effects of both the EMP and the QE field has recently been developed [*Pasko et al.*, 1998a]. In this paper, we describe this model, and we apply it to investigate the temporal structure of elves as measured from different points of view. In particular, we discuss the dependence of optical emissions on the rise and fall times of the current waveform. We also examine the temporal structure of optical emissions as a function of different observational geometries. We calculate the response curves as would be observed with finite field of view photometers having different elevation and azimuth angles. Finally, we apply the new model to calculate ionization changes and optical emissions associated with long duration lightning flashes leading to sprites.

2. Model Formulation

In this section we separately describe the new electromagnetic model and the optical emission calculation algorithms for different viewing geometries.

2.1. Electromagnetic Model of the Lightning-Ionosphere Interaction

We use a cylindrical coordinate system (r,ϕ,z), where the z axis represents altitude, and assume no azimuthal dependence $(\partial/\partial\phi = 0)$. Our numerical simulation box extends from z=0 km to z=100 km and from r=0 km to r=400 km, with grid spacings of Δz=0.5 km and Δr=2 km. We assume perfectly conducting boundaries at z=0 km, z=100 km and r=400 km. The peak spectral content of lightning radiated electromagnetic fields is in the VLF range $(3-30$ kHz) [*Uman*, 1987, p. 118]. In this frequency range the ground can be assumed to be perfectly conducting. Strong attenuation and reflection in the lower ionospheric layers (< 95 km) results in a negligible amount of energy penetrating to altitudes > 95 km [*Taranenko et al.*, 1993a] and justifies perfectly conducting (reflecting) boundary at 100 km altitude. Additional tests were performed indicating that results are insensitive to position of the upper boundary. The radial perfectly conducting boundary at r=400 km has no effect on the accuracy of our results, due to the fact that the radiated field pattern consists of an expanding cylindrical shell [*Inan et al.*, 1996b] which produces negligible optical emissions for r >300 km. In addition, we limit the simulation time to the time required for the radiated field to propagate to radial distances of ~400 km and thus exclude unphysical effects of reflections caused by the radial boundaries.

The electric and magnetic fields are calculated using the following system of equations:

$$\frac{\partial E_z}{\partial t} = -\frac{J_s}{\varepsilon_o} - \frac{\sigma E_z}{\varepsilon_o} + c^2 \frac{1}{r}\frac{\partial}{\partial r}(rB_\phi) \quad (1)$$

$$\frac{\partial E_r}{\partial t} = -\frac{\sigma E_r}{\varepsilon_o} - c^2 \frac{\partial B_\phi}{\partial z} \quad (2)$$

$$\frac{\partial B_\phi}{\partial t} = \frac{\partial E_z}{\partial r} - \frac{\partial E_r}{\partial z} \quad (3)$$

where $\vec{J}_s = J_s(r,z,t)\hat{\mathbf{z}}$ is the return stroke current density. We use these equations since only transverse magnetic fields are excited in our system by the source current density.

We adopt previously used models of ambient electron number density, ambient ion conductivity and ambient neutral density profiles [*Pasko et al.*, 1997]. The Earth's magnetic field is neglected, since even under mild heating conditions the effective collision frequency of the electrons is much larger than the electron gyrofrequency. The conductivity σ in (1) and (2) is calculated self-consistently by taking into account the effect of the electric field on electrons through changes in mobility (due to heating) and electron density (due to attachment and/or ionization). We use the electron mobility, ionization and attachment coefficients derived from kinetic models and swarm experiments [*Pasko et al.*, 1997]. The ionization ν_i and attachment ν_a coefficients are used to calculate electron density changes using

$$\frac{dN_e}{dt} = (\nu_i - \nu_a)N_e \quad (4)$$

The expressions used for mobility, ionization and attachment coefficients are valid for lightning radiated EM fields exhibiting relatively slow time variations (less than ~10 μs) [*Taranenko et al.*, 1993a]. However, *Glukhov and Inan* [1996] showed that even in the case of rapid variations of the lightning-induced fields (risetime of a few microseconds) the resultant optical emissions are very similar to those calculated using the quasi-stationary model [e.g., *Taranenko et al.*, 1993a].

The source current density $\vec{J}_s$ has smooth spatial variation in both r and z. The spatial distribution is given by

$$J_s = J_{s0}e^{-r^2/r_0^2}, \quad z < a$$

$$J_s = J_{s0}e^{-r^2/r_0^2-(z-a)^2/z_0^2}, \quad z > a$$

where a=10 km, r_0=3Δr, z_0=3Δz, so that the total source current is $I_s(t) = \int J_s(\vec{r},t)dS$. The time dependence of the total source current is described by the relation

$$I_s(t) = I_p\frac{t}{\tau_r}, \quad t < \tau_r$$

$$I_s(t) = I_p e^{-[(t-\tau_r)/\tau_f]^2}, \quad t > \tau_r$$

where τ_r is the current waveform risetime, τ_f is the fall time and I_p is the peak current at $t = \tau_r$. The current I_p is available experimentally from measurements of the National Lightning Detection Network (NLDN) [e.g., *Idone et al.*, 1993]. We note that the actual duration of the lightning flashes as well as the functional time dependence of the total source current are not available from measurements provided by NLDN. However, these parameters constitute critically important inputs for modeling lightning-ionosphere interactions. The above choice of the functional dependence of $I_s(t)$ is quite realistic and consistent with the observed current waveforms of lightning return strokes [*Uman*, 1987, p. 122]. By properly selecting the parameters τ_r and τ_f we are able to investigate a variety of different current waveforms. The thundercloud charge removed from cloud to ground over a time t is calculated using the relation $Q(t) = \int_0^t I_s(t)\,dt$.

We solve (1)-(4) using space and time centered finite differences [*Birdsall et al.*, 1991, p. 353]. For the time integration we use a modified version of the leap-frog scheme described by *Birdsall et al.* [1991, p. 353], which is sketched in Figure 1a. The electric field has to be advanced by a half time step (from $n - \frac{1}{2}$ to n) before the conduction current is calculated in (1) and (2). The relative spatial locations of the field components are chosen as sketched in Figure 1b and provide centered spatial differencing. Equation (4) has to be integrated in time both at n and $n+\frac{1}{2}$ time steps (Figure 1a), since the conduction current has to be calculated at both time steps. N_e at n time steps is used in the calculation of the conduction current in (1) and (2), while N_e at $n+\frac{1}{2}$ time steps is used in the half time step advancement of the electric field. Figure 1c shows the simulation box.

Several considerations have to be taken into account in the selection of the appropriate time step for the numerical model. First, the time step Δt must satisfy the Courant condition [*Birdsall et al.*, 1991, p. 355], namely $\Delta t < c^{-1}[(\Delta r)^{-2} + (\Delta z)^{-2}]^{-1/2}$ so that no nonphysical damping or growth occurs. In addition, since the quasi-electrostatic component of the lightning field is included in our model the time step is limited to be less than the minimum relaxation time of the medium ($\Delta t < (\varepsilon_o/\sigma)_{\min}$). This constraint is the major limitation to the numerical efficiency of our model, owing to the vast differences (many orders of magnitude) between the ambient conductivity of the medium at low altitudes versus ionospheric altitudes [e.g., *Inan et al.*, 1996d]. Finally, since (4) is used to calculate the temporal dynamics of the electron density, the time step must satisfy the condition $\Delta t < 1/\nu_{i,a\max}$.

In order to check the validity of our model, we made several comparisons with previous models of the lightning-

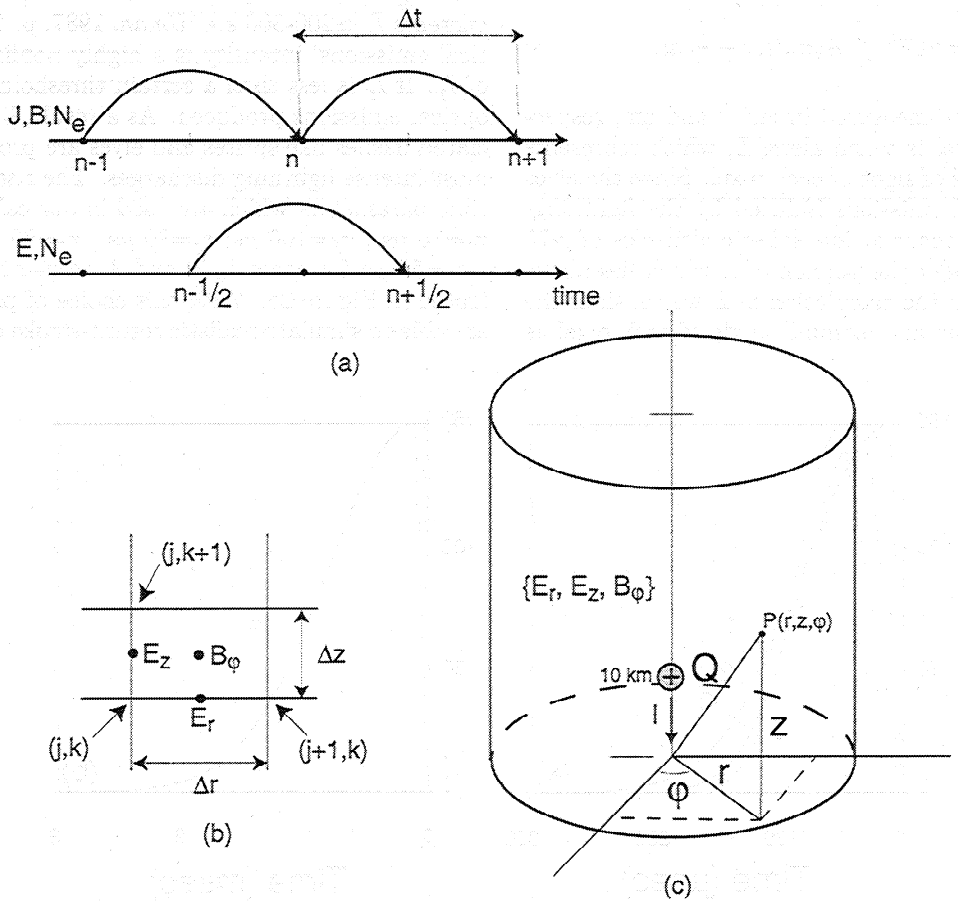

Figure 1. (a) Temporal layout of quantities used in the leapfrog integration; (b) location of the field components on the spatial grid; and (c) simulation box.

ionosphere coupling. We compared results obtained with the new model with those from both the EMP-ionosphere interaction models [e.g., *Inan et al.*, 1996, 1997] and from the QE models [e.g., *Pasko et al.*, 1997]. In all cases we obtained almost identical results.

2.2. Optical Emission Calculation Algorithms

Once the electric field and the electron density are calculated via the electromagnetic model described in the previous paragraph, the intensities of the various optical emissions are determined. We consider the first positive band of N_2, since the photometers' signal is expected to come primarily (> 90%) from this band [*Inan et al.*, 1997; *Pasko et al.*, 1997; *Taranenko et al.*, 1993b]. The effects of Rayleigh scattering and narrow-band molecular line absorption are not taken into account. The number density of excited particles n_k in state k is governed by the relation:

$$\frac{\partial n_k}{\partial t} = -\frac{n_k}{\tau_k} + \sum_m n_m A_m + \nu_k N_e \qquad (5)$$

where the optical excitation coefficients ν_k obtained from kinetic calculations as a function of the electric field, and the total lifetime τ_k of state k, and the radiation transition rate A_k can be found in the work of *Pasko et al.* [1997].

The intensity of optical emissions in Rayleighs is given by the expression [*Chamberlain*, 1978]

$$I_k(t) = 10^{-6} \int_L A_k n_k(l, t - \frac{l}{c}) dl, \qquad (6)$$

where n_k and l are measured in cm^{-3} and cm, respectively. The integral is taken along L, which represents the individual line of sight of each pixel. Since the elves associated optical emissions induced by the lightning-EMP interaction occur at ionospheric altitudes of >75 km, we only consider the portion of L which lies above 70 km altitude. In the calculation of L we consider the individual elevation and azimuth angle of each pixel as well as the distance of the photometer from the center of the coordinate system. Since this distance is usually of the order of several hundreds of kilometers, it is essential to take into account the curvature of the Earth. We also note that the photons that arrive at a pixel at time t_0, originating from a point within the line of sight at a distance l from the pixel, were emitted at $t = t_0 - l/c$.

2.3. Model Parameters

We use the typical midlatitude night ion conductivity profile from [*Hale*, 1994] and the electron density profile 1 employed by *Pasko et al.* [1997].

Since we are interested in studying the effect of current waveform on optical emissions, we consider variable risetime and fall time return stroke current waveforms. By properly selecting the parameters τ_r and τ_f we are able to investigate a wide range of current waveforms. We first consider three different cases as illustrated in Figure 2a. We choose the parameters τ_r and τ_f so that the total duration of current pulses in all three cases is approximately the same. The total duration chosen (~100 μs) is consistent with the typical return stroke duration of real lightning discharges [*Uman*, 1987, p. 124]. We perform calculations for peak current I_p=150 kA, the choice of which is justified by the NLDN-estimated peak currents of lightning flashes associated with elves [*Inan et al.*, 1997]. I_p > 100 kA is rare for negative CG flashes. However, positive CG discharges are usually more intense and may have peak currents $I_p \simeq$200-300 kA [*Uman*, 1987, p. 200]. The optical emissions' intensity is a highly nonlinear function of I_p. If I_p is less than a certain threshold there are no optical emissions produced. As a result, lightning associated flashes like sprites and elves are produced by the most intense lightning discharges. The risetime and fall time parameters which are used in our calculations are τ_r=10 μs , τ_f=100 μs; τ_r=30 μs , τ_f=70 μs; τ_r=50 μs , τ_f=50 μs for cases 1, 2, and 3, respectively, as illustrated in Figure 2a. With this choice of parameters we are able to simulate realistic return-stroke current wave-

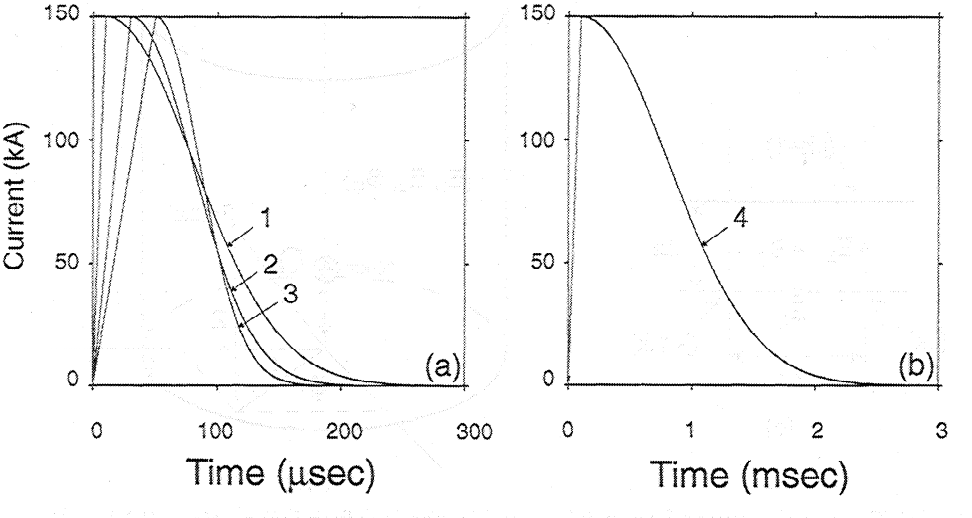

Figure 2. The four current waveforms used in calculations.

shapes which most commonly have two distinct parts: an initial surge reaching a peak value over a timescale of a few microseconds followed by a more gradual change over a timescale of ~100 μs [*Uman*, 1987, p. 122].

The risetimes and fall times chosen for the three current waveforms are characteristic of negative lightning flashes. In the case of a positive lightning typical current waveform parameters are quite different from those listed above. Positive lightning discharges have slower current risetimes and much slower current fall times than do negatives [*Uman*, 1987, p. 199]. As a result, the total flash duration is typically many times larger in positive cloud to ground (CG) discharges and the total charge removed is over an order of magnitude larger for positive than for negative single-stroke flashes [*Uman*, 1987, p. 200]. In order to illustrate the effects of positive lightning, we consider a fourth current waveform with τ_r=100 μs , τ_f=1 ms and I_p=150 kA, as illustrated in Figure 2b. Optical emissions associated with these flashes (case 4) exhibit quite distinct characteristics from optical emissions associated with discharges of short duration current waveforms (cases 1, 2, and 3), as we discuss in detail below.

The geometry of the model problem is illustrated in Figure 3. The observer is located 700 km from the center of the coordinate system. At this distance the ground under the lightning return stroke is ~38 km below the horizon from the point where the observer is located. As a result, neither light generated directly by the lightning flash nor cloud-scattered light would be visible from the location of the observer and the only visible flashes would be those associated with the lightning-mesosphere/lower ionosphere interaction. We calculated the lightning induced optical emissions that

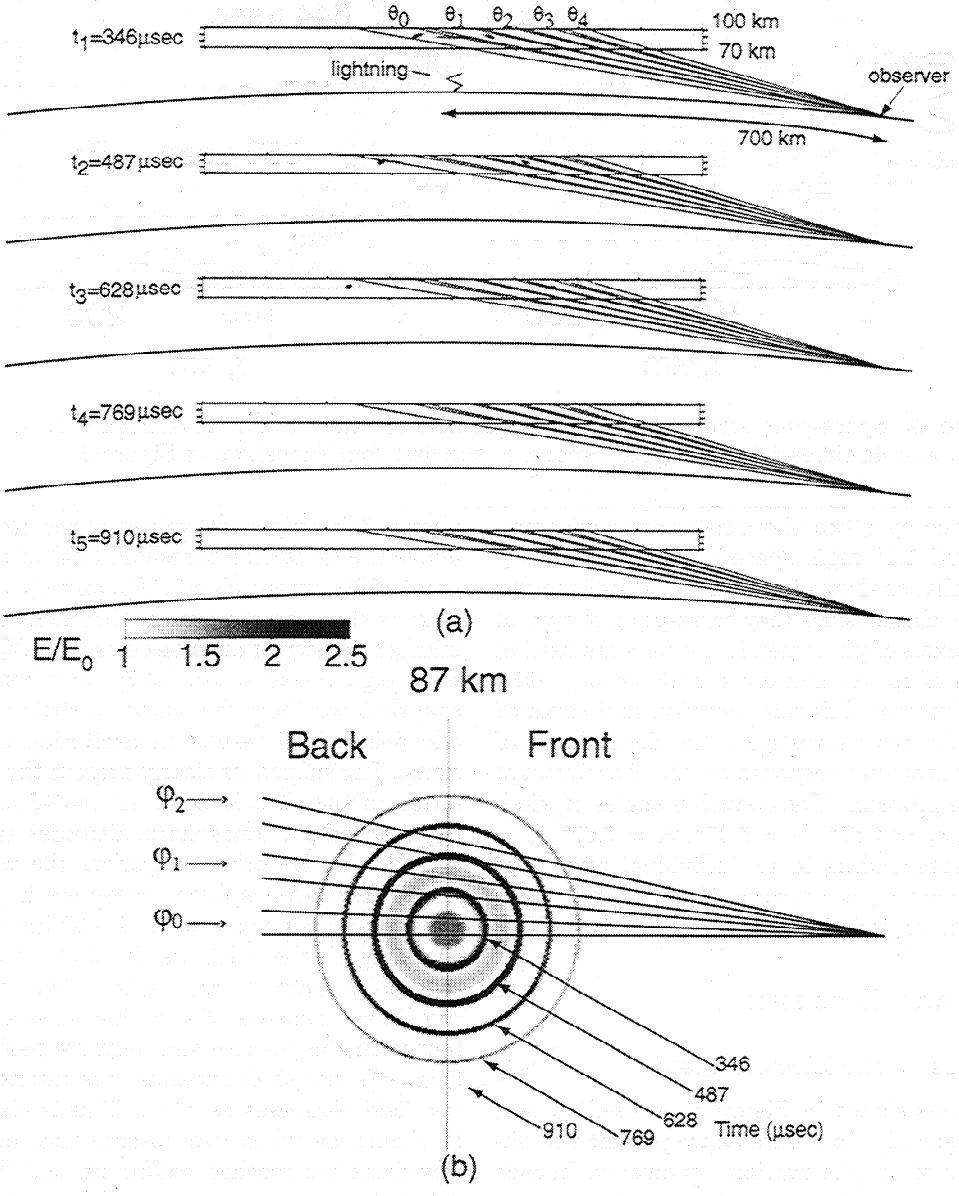

Figure 3. Observation geometry of the problem. E_0 is the the excitation threshold of the first positive band of N_2.

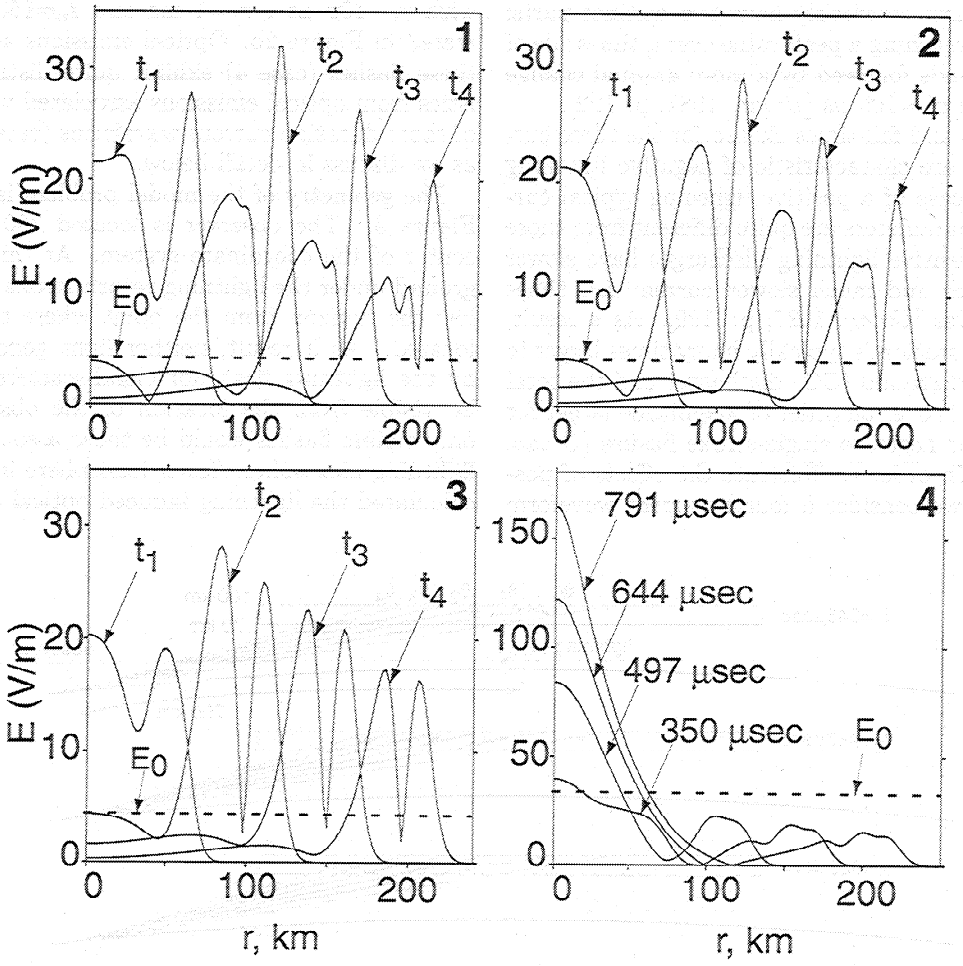

Figure 4. Space-time structure of the electric field for the waveforms of Figure 2. In Figures 4a, 4b, and 4c times t_1, t_2, t_3, t_4 correspond to the first four snapshots of Figure 3.

would be recorded by a 3×5 photometer array with pixels 2.2° wide and 1.1° high, spaced by 5° horizontally and 1.4° vertically, as shown in Figure 3. These angular dimensions were chosen since they correspond to typical dimensions of pixels of photometric instruments used in the observation of sprites and elves [*Inan et al.*, 1997]. Each pixel is aimed at different elevation and azimuth angles, to enable us to investigate the dependence of the observed photometer response on the observational geometry of the problem. The elevation angles of pixels are $\theta_0 = 3.47°, \theta_1 = 4.87°, \theta_2 = 6.27°, \theta_3 = 7.67°, \theta_4 = 9.07°$, each corresponding to an individual row. The azimuth angles are $\phi_0 = 0°, \phi_1 = 5°, \phi_2 = 10°$, each corresponding to an individual column (Figure 3).

3. Results and Discussion

3.1. Dynamics of the Electric Field

For calculations shown in Figure 3 we used current waveform 1 (Figure 2). In Figure 3a we present five different snapshots of the observational geometry. In each snapshot we show the altitude and radial distribution of the total electric field for $z > 70$ km, since elves occur at ionospheric altitudes of > 75 km as was mentioned above. We only show values of the total electric field above the excitation threshold (E_0) of the first positive band of N_2, where $E_0 \simeq 0.3E_k$, and $E_k = 3.2 \times 10^6 N/N_o$ V/m is the characteristic air breakdown field, N is the number density of air molecules, and $N_o = 2.688 \times 10^{25}$ m^{-3} [e.g., *Pasko et al.*, 1997]. In other words, in each snapshot we show the spatial distribution of the electric field which results in excitation of optical emissions. The snapshots clearly present the space-time evolution of the electric field. At t=346 μs the wavefront has reached the ionospheric altitudes and has been reflected. In the other snapshots the wave propagates in the Earth-Ionosphere waveguide in the form of an expanding cylindrical shell of ~60 km thickness corresponding to the ~200 μs duration of the source current pulse [*Inan et al.*, 1996c]. The expanding cylindrical shell consists of a double pulse structure consistent with the positive and negative peak of the electric field. As the shell expands, the intensity of the electric field decreases as r^{-1} . This is clearly illustrated in Figure 3a where we observe that at t=910 μs the wavefront has reached $r \simeq 250$ km and the peak electric field is just above the threshold for excitation of optical emissions. When the wavefront reaches $r \simeq 300$ km (not shown) the peak electric field is below the threshold, in-

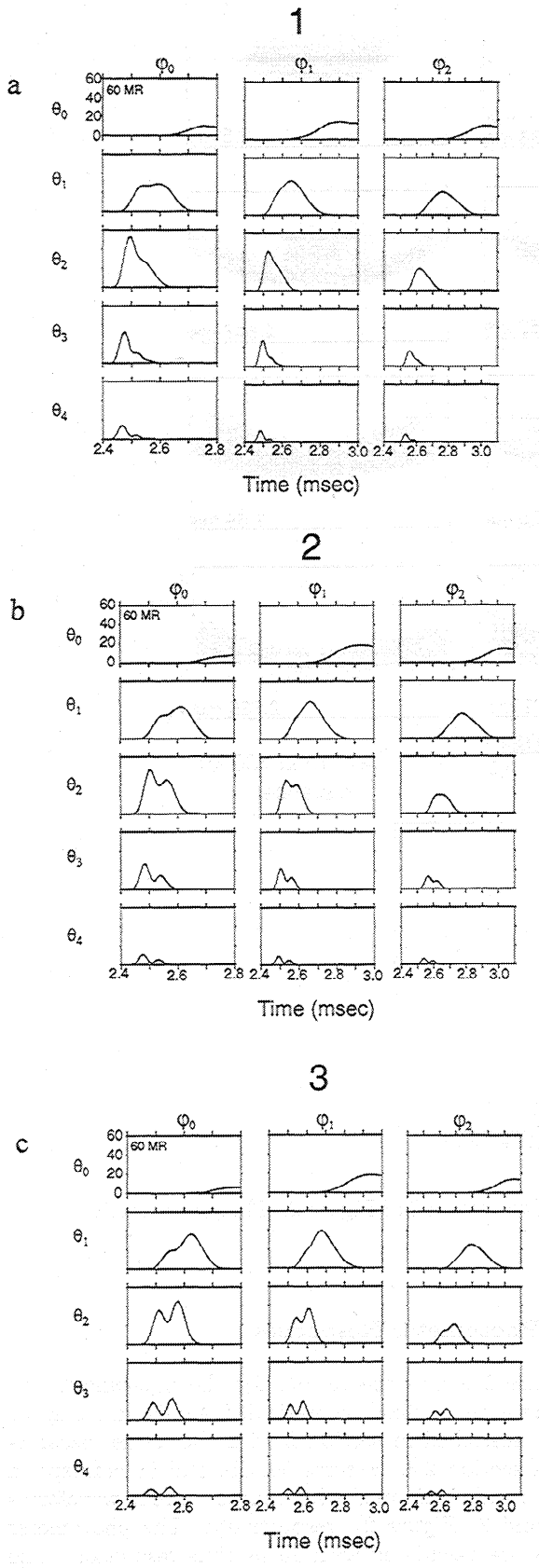

Figure 5. Photometric responses for pixel $P_{ij}, i = 0..4, j = 0..2$. Figures 5a, 5b, and 5c present results for waveforms 1, 2, and 3 of Figure 2 respectively.

dicating that the lateral extent of the luminous region does not exceed ~600 km [*Inan et al.*, 1997]. It should also be noted that the radiation field intensity has a minimum directly above the source current [*Inan et al.*, 1997]. During the reflection process the peak electric field increases and when the double peak structure is formed the peak electric field is maximized, afterwards decreasing with the r^{-1} dependence. Thus, for small r the field intensity is an increasing function of r, it is maximized when the double-pulse cylindrical structure of the electric field is formed, and it decreases with the r^{-1} dependence as this cylindrical shell structure expands. This variation of the peak field intensity is reflected in the observed optical emissions, as we discuss below. The photometer pixels with different elevation angles receive photons excited by different portions of the electric field pattern at different times. This will be discussed in detail in section 3.2.

The space-time structure of the electric field for a different current waveform is similar to the described above with the exception that the relative magnitudes of the two pulses in the expanding cylindrical shell are different. The lightning-radiated field has a positive and a negative peak. This is consistent with the fact that the electric field is proportional to the time derivative of the current waveform. Thus the relative magnitudes of the two pulses in the electric field structure at ionospheric altitudes are dependent on the risetime and fall time of the source current waveform. This is illustrated in Figure 4 where we plot the absolute value of the electric field at altitude z=87 km as a function of radial distance and at different instants of time for current waveshapes 1, 2, and 3. We observe that for waveform 1 the first pulse is much bigger than the second, while for waveform 3, which has a substantially bigger risetime τ_r the two pulses have almost the same magnitude. The shape of the electric field waveform is reflected in the observed optical emissions, as we discuss below. The intensity of the radiated electric field decreases as r^{-1} in all 3 cases because of the radial expansion of the shell structure. In Figure 4 we also present for comparison the electric field structure at z=75 km for current waveform 4 (Figure 2b), which, as we mentioned above, simulates long duration positive lightning flashes. In this case we observe that the central quasi-electrostatic component of the total electric field dominates the radiation one. The radiation component, although several times smaller than the quasi-electrostatic component, is still present. We also note that, while the radiation component decreases as the wave propagates as a result of the expansion of the cylindrical shell, the quasi-electrostatic component increases as more charge is removed by the lightning discharge. Optical emissions associated with the quasi-electrostatic component of the electric field dominate in the case of long-duration lightning flashes, as we discuss below. In cases 1, 2, and 3 we observe that the radiation component dominates and the quasi-electrostatic is almost negligible, especially as far as optical emissions are concerned.

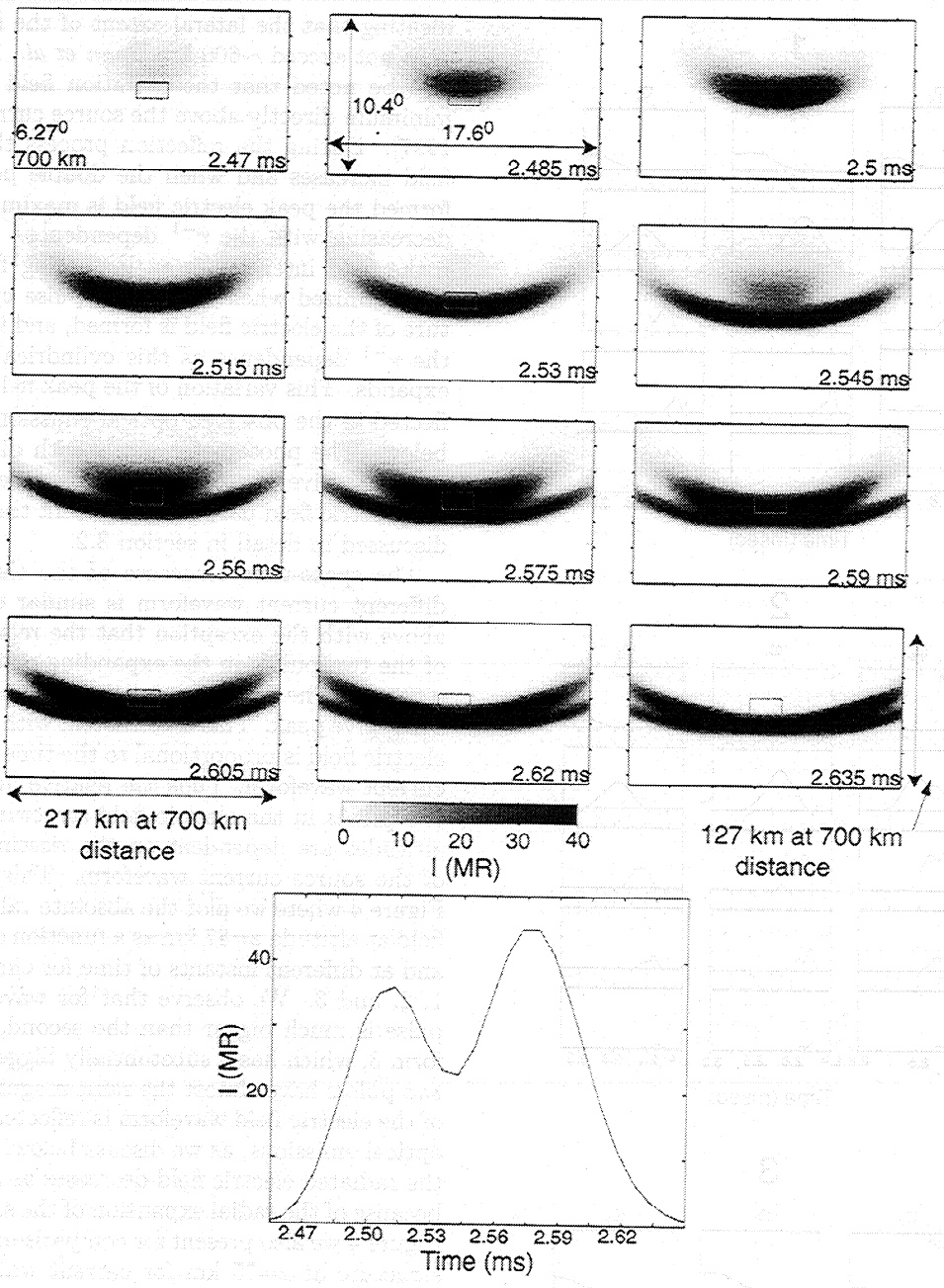

Figure 6. View of the sky with a camera for the case of waveform 3 of Figure 2. The photometric response of pixel P_{20} is also illustrated for comparison.

In Figure 3b we show snapshots of the same electric field pattern at z=87 km in horizontal cross section. We observe that pixels with different azimuth angles view different portions of the expanding cylindrical shell. The variations of the peak field amplitude as the shell expands are well illustrated in Figure 3b. We observe the minimum field amplitude at the center of the system, the maximum when the double-pulse structure is formed and the r^{-1} decrease as the wave propagates. Figure 3b also shows that the expanding shell consists of the front and back part with respect to the observer. This distinction [*Inan et al.*, 1996c] will be further discussed in section 3.2.

3.2. Photometer Responses

Figure 5 shows the results for the photometric responses for each pixel theoretically calculated using the model described in section 2 with the model parameters of section 2.3. Figures 5a, 5b, and 5c correspond to the results obtained with source current waveforms 1, 2, and 3 (Figure 2), respectively. The photometer signals are calculated with 10 μs time resolution. The vertical axes show intensity in MR and are identical for all pixels. The time axes show milliseconds after the onset of the source current waveform. The time axes are identical for pixels with the same azimuth angle. For

convenience, we will refer to the pixel with elevation angle θ_i and azimuth angle ϕ_j as P_{ij}. The θ_i and ϕ_j values are the elevation and azimuth angles shown in Figure 3. In the following we discuss the main characteristics of the photometric responses.

3.2.1. Onset of photometric signal. We observe that the onset of the response is not the same for all pixels, although it clearly does not depend on current waveform. Each photometric pixel has a narrow field of view and only a small part of the expanding electric field pattern at ionospheric altitudes of ~90 km (altitude range at which optical emissions occur) (Figure 3b) lies inside its field of view. The onset delay of the signal of each pixel with respect to the onset of the source current waveform is equal to the travel time of the electromagnetic wave from the lightning discharge to the field of view of the pixel plus the travel time of the emitted light from that point to the observer. Because of the geometry of the system, the onset delay is almost the same for points in the front of the expanding shell (Figure 3b), while it increases with distance from the center of the system for points in the back. This effect leads to focusing of light from the front and defocusing of the light from the back [*Inan et al.*, 1996c]. Thus we observe that the signals of pixels P_{20}, P_{30}, P_{40} which aim at the front have almost simultaneous onset. However, the signals of pixels P_{00} and P_{10},which aim at the back, have increased onset delay with respect to P_{20}, P_{30}, P_{40}. The onset for other pixels can be similarly interpreted.

3.2.2. Duration of photometric signal. The duration of the photometric signal for each pixel depends on the azimuth and elevation angles of the pixel and it does not depend on the current waveform. For a pixel P aimed at the front, photons emitted at different points inside its field of view arrive simultaneously at P because of focusing. Thus, the duration of the optical signal is approximately equal to the duration of the electric field pattern. We observe that the signal duration of P_{20}, P_{30}, P_{40} is roughly ~200 μs which is equal to the duration of the electric field pattern. However, for a pixel P aimed at the back, photons emitted at different points inside its field of view arrive at different times at P because of 'defocusing'. Thus, the duration of the optical signal is approximately equal to the duration of the electric field pattern plus the maximum difference of arrival times for photons emitted at different points inside the field of view. We observe that the signal duration of P_{00}, P_{01}, P_{02} is much longer than the current waveform duration as a result of defocusing. This is one of the main reasons that the current waveform shape is not reflected in these pixels' signals, as we discuss below.

3.2.3. Peak intensity of photometric signal. The peak intensity of the photometric signals depends mainly on two factors. As we discussed above, only a small portion of the electric field pattern lies inside the narrow field of view of each pixel. Clearly, the peak intensity of the photometric signal depends nonlinearly on the peak of the electric field crossing the pixel's field of view. However, pixels aimed at portions of the electric field pattern with the same peak intensity do not necessarily have the same peak intensity of optical signal. This is again due to the effect of focusing and defocusing. Thus the fact that the peak intensity of P_{00} is smaller by a factor of ~5 with respect to the peak intensity of P_{10} is due to defocusing of light for P_{00} compared to focusing of light for P_{10}. However, the difference in peak intensities for P_{20}, P_{30}, P_{40} is due to the r^{-1} attenuation of the peak electric field intensity.

In a similar way we can interpret the reduction of peak intensities with increasing azimuth for pixels in rows 2, 3, and 4 which is not observed for pixels in rows 0 and 1. Pixels with increasing azimuth have increasing distances of their field-of-view from the center of the system. However, the peak intensity of the electric field as we discussed above is not a monotonically decreasing function of distance. In the center of the electric field pattern, the peak electric field intensity is increasing with increasing distance, while at the sides it is decreasing. For example, pixels P_{20}, P_{21} are aimed at the sides. Thus, the peak intensity of P_{21} is smaller than the peak intensity of P_{20} because of the r^{-1} attenuation of the peak electric field intensity. However, pixels P_{00}, P_{01} are aimed at the center of the system. Thus the bigger distance of the field of view of P_{01} from the center of the system results in bigger peak electric field intensity and thus bigger photometric signal intensity.

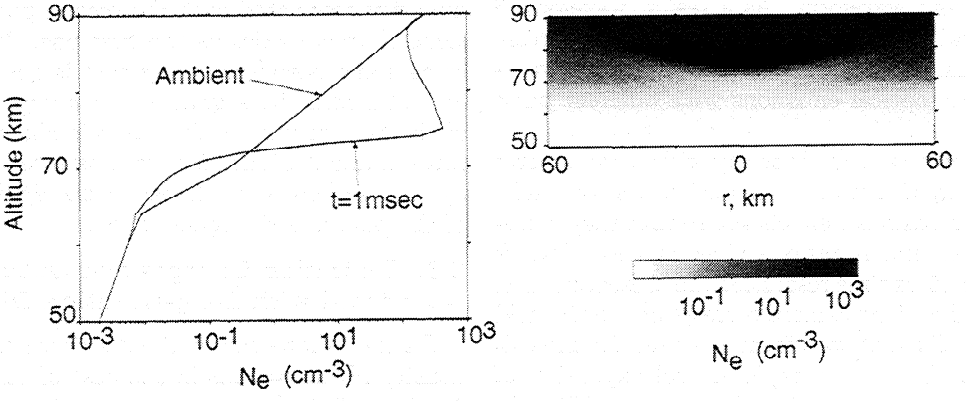

Figure 7. The altitude distribution of electron density N_e for the case of waveform 4 at $t = 1$ ms.

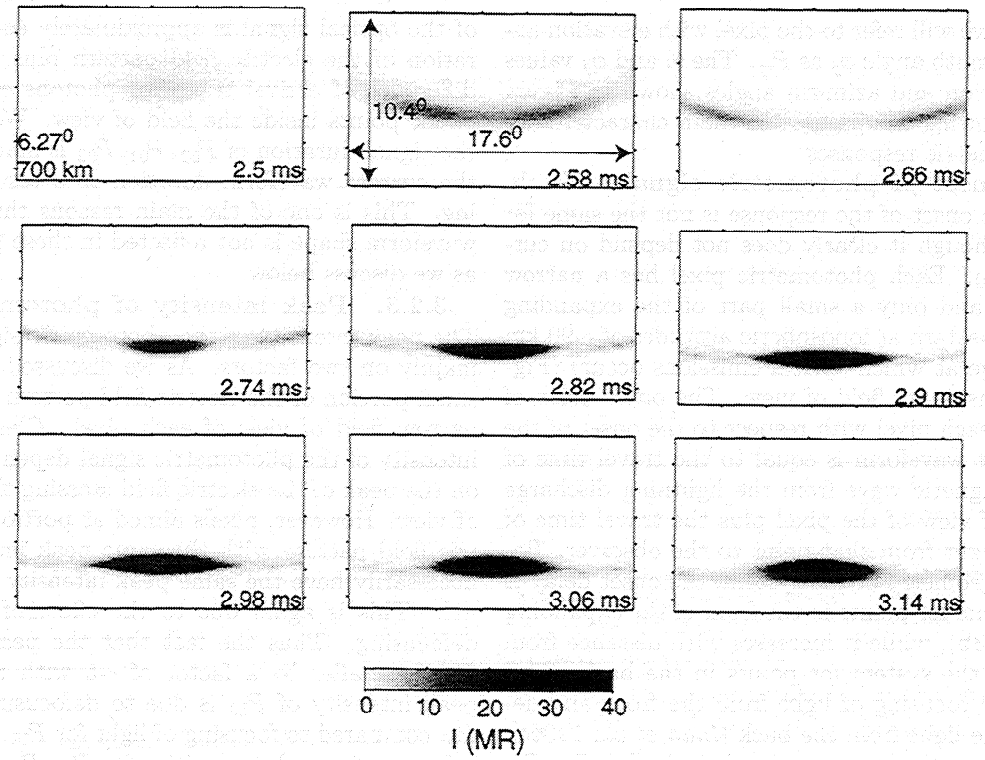

Figure 8. View of the sky with a camera for the case of waveform 4 of Figure 2.

3.2.4. Shape of photometric signal. As we mentioned above, the current waveform shape is not reflected in the signals of P_{00}, P_{01}, P_{02} because of defocusing. Thus we observe that the signals for these pixels are almost the same for waveforms 1, 2, and 3 (Figure 2). The current waveform is also not reflected in the signals of P_{10}, P_{11}, P_{12}. This is due to the fact that these pixels are aimed at the center of the system where the reflection occurs and the double peak structure has not yet been formed. On the contrary, we observe that the current waveform shape is clearly reflected in pixels in rows 2, 3, and 4. Their shape depends on the shape of the electric field pattern. Thus we see that their signals consist of two pulses. The relative magnitudes of these optical pulses depend on the relative magnitudes of the pulses of the electric field structure which in turn depend as we discussed above on the rise and fall times of the source current waveform. As a result, waveform 3 produces optical emissions with double pulse structure and almost equal relative pulse magnitudes, while waveform 1 produces optical emissions with different pulse magnitudes.

Figure 6 shows the view of the sky with a photometer with a broad field of view aimed at 6.27° elevation angle. The angular dimensions were chosen so that they correspond to typical dimensions of a video camera. Twelve snapshots with 15 μs time resolution are presented. The box in the middle of the camera corresponds to the field of view of P_{20}. Current waveform 3 is used for the calculations. We observe the rapid lateral expansion of the observed optical luminosity [*Inan et al.*, 1997]. At t=2.47 ms the photons emitted from the front of the emission shell begin to reach the field of view of the camera. As more photons arrive from the front, the optical emissions intensities increase, as is observed in the second and third frame. The light arriving from the front gradually decreases, while the light emitted from the back begins to reach the camera. Since the back corresponds to lower elevation angles, as observed by the camera, the optical luminosity appears to move downwards, as observed in the fourth and fifth frame. As a result, the photometric signal of P_{20}, whose field of view is in the center of the camera, decreases. As we already mentioned, the two pulses in the expanding cylindrical shell of the electric field structure result in a similar structure of the optical emission region. Thus, at t=2.545 ms light from the second pulse of the optical emission structure begins to reach the camera and the photometric signal of P_{20} increases. The optical luminosity associated with the second pulse exhibits the same characteristics as the first one. Its intensity increases and downward movement is observed. The two optical luminosities gradually converge and move out of the field of view of P_{20}, as it is observed in the last three frames. Figure 6 thus illustrates the space-time dynamics of elves which lead to the double-pulse shape of the photometric signal of P_{20}.

3.3. Ionization Changes and Optical Emissions Associated with Long-Duration Discharges

Figure 7 shows the spatial distribution of the electron density N_e at t=1 ms in the case of current waveform 4 (Figure 2b). Intense ionization changes are observed above ~70 km altitude. As we mentioned above, the

quasi-electrostatic component of the electric field dominates in this case. As charge is removed by the discharge, the large QE field develops slowly and exceeds the breakdown threshold E_k above 70 km altitude. At lower altitudes attachment dominates leading to electron density decreases below ambient values. The transverse extent of the disturbed region is ~100 km.

Figure 8 presents the view of the sky with a camera with a broad field of view aimed at 6.27°. The observational geometry is exactly the same as in Figure 6. However, current waveform 4 is used instead of waveform 3 for the calculations. Thus, we are able to compare optical emissions associated with long-duration lightning flashes with optical emissions of short-duration lightning flashes. As we mentioned above, in short-duration lightning flashes the radiation component of the electric field dominates, while in long-duration discharges the quasi-electrostatic component dominates. This is reflected in the optical emissions. We observe that the structure of the optical luminosity when current waveform 4 is used (quasi-electrostatic case) is initially very similar to the optical emissions structure of Figure 6, although the intensities are smaller. The weak optical luminosity observed in the first frames is associated with optical emissions excited by the small radiation component of the electric field. However, at t=2.74 ms light generated by the strong quasi-electrostatic component of the electric field begins to reach the camera. An intense optical luminosity appears in the camera and gradually increases, as more charge is removed by the lightning discharge. This luminosity associated with the quasi-electrostatic component of the electric field does not appear in Figure 6, since in the case of short lightning discharges the quasi-electrostatic field is small and below the excitation threshold of optical emissions. The intensity of the luminosity generated by the quasi-electrostatic component of the electric field is a highly nonlinear function of the total removed charge Q [*Pasko et al.*, 1997]. In the case of Figure 6, where waveform 3 is used, the total removed charge is $Q \simeq 10.4$ C and optical emissions generated by the quasi-electrostatic component are negligible. In the case of Figure 8, where waveform 4 is used, the total removed charge is $Q \simeq 140.4$ C and optical emissions associated with the quasi-electrostatic component dominate. The highly nonlinear dependence of optical emissions on the total removed charge is due to the threshold-like behavior of the optical excitation cross sections [*Pasko et al.*, 1997]. The intense optical luminosity generated by the quasi-electrostatic field in the case of Figure 8, does not resemble filamentary sprite structure observed in video. This is due to the fact that it is not computationally possible to resolve the small-scale sprite optical structure in the model used in the present paper (i.e., using spatial grids ~1 km). One needs to have very fine resolution to be able to model the fine spatial structure of sprites (see *Pasko et al.* [1998b] and further discussion by *Pasko et al.* [1998a]). On the other hand, large-scale characteristics of the space-time dynamics of optical emissions generated by the quasi-electrostatic field such as the altitudes at which they occur, their lateral extent and their duration are in good agreement with those of sprites.

4. Summary

We have used a new model of lightning-ionosphere interaction which includes the effects of both EMP and QE fields to study the characteristics of optical flashes observed under different viewing geometries. In particular, we have considered short-duration lightning flashes (~100 μs) characterized by distinct rise and fall components of lightning current, for which the electric field pattern is an expanding cylindrical shell consisting of a double-pulse structure. In this case the radiation component of the electric field dominates above the quasi-electrostatic component and the relative magnitudes of the two pulses depend on the risetime and fall time of the current waveform. The dynamics of the electric field are reflected in the optical emissions produced by lightning discharges. Optical emissions are sensitive to both the observational geometry and the current waveform. For short-duration flashes with risetime of ~50 μs or longer the space-time dynamics of optical emissions lead to double-pulse shape of the signal observed with a photometer.

For long-duration flashes (~1 ms) optical emissions generated by the quasi-electrostatic component of the electric field dominate above those produced by the radiation (EMP) component.

Acknowledgments. This work was sponsored by the NSF grant ATM-9731170 to Stanford University. We greatly appreciate consultations with Slava Glukhov on optical emission calculation algorithms.

Janet G. Luhmann thanks Alexander Sukhorukov and another referee for their assistance in evaluating this paper.

References

Birdsall, C. K., Langdon A. B., *Plasma Physics via Computer Simulation*, Adam Hilger, London, 1991.

Chamberlain, J. W., *Theory of Planetary Atmospheres*, Academic, San Diego, Calif., 1978.

Fishman, G. J., et al., Discovery of intense gamma-ray flashes of atmospheric origin, *Science, 264*, 1313, 1994.

Fukunishi, H., Y. Takahashi, M. Kubota, K. Sakanoi, U. S. Inan, and W. A. Lyons, Lightning-induced transient luminous events in the lower ionosphere, *Geophys. Res. Lett., 23*, 2157, 1996.

Glukhov, V. S., and U. S. Inan, Particle simulation of the time-dependent interaction with the ionosphere of rapidly varying lightning EMP, *Geophys. Res. Lett., 23*, 2193, 1996.

Hale, L. C., Coupling of ELF/ULF energy from lightning and MeV particles to the middle atmosphere, ionosphere, and global circuit, *J. Geophys. Res., 99*, 21089, 1994.

Idone, V. P., A. B. Saljoughy, R. W. Henderson, P. K. Moore, and R. B. Pyle, A reexamination of the peak current calibration of the National Lightning Detection Network, *J. Geophys. Res., 98*, 18323, 1993.

Inan, U. S., T. F. Bell, and J. V. Rodriguez, Heating and ionization of the lower ionosphere by lightning, *Geophys. Res. Lett., 18*, 705, 1991.

Inan, U. S., A. Slingeland, V. P. Pasko, and J. Rodriguez, VLF signatures of mesospheric/ lower ionospheric response to lightning discharges, *J. Geophys. Res., 101,* 5219, 1996a.

Inan, U. S., S. C. Reising, G. J. Fishman, and J. M. Horack, On the association of terrestrial gamma-ray bursts with lightning discharges and sprites, *Geophys. Res. Lett., 23,* 1017, 1996b.

Inan, U. S., W. A. Sampson, and Y. N. Taranenko, Space-time structure of lower ionospheric optical flashes and ionization changes produced by lightning EMP, *Geophys. Res. Lett., 23,* 133, 1996c.

Inan, U. S., V. P. Pasko, and T. F. Bell, Early/Fast VLF events as evidence of sustained heating of the ionosphere above thunderclouds, *Geophys. Res. Lett., 23,* 1067, 1996d.

Inan, U. S., C. Barrington-Leigh, S. Hansen, V. S. Glukhov, T. F. Bell, and R. Rairden, Rapid lateral expansion of optical luminosity in lightning-induced ionospheric flashes referred to as 'elves', *Geophys. Res. Lett., 24,* 583, 1997.

Pasko, V.P., U. S. Inan, T. F. Bell, and Y. N. Taranenko, Sprites produced by quasi-electrostatic heating and ionization in the lower ionosphere, *J. Geophys. Res., 102,* 4529, 1997.

Pasko, V.P., U.S. Inan, and T.F. Bell, Mechanism of ELF radiation from sprites, *Geophys. Res. Lett., 25,* 3493, 1998a.

Pasko, V.P., U.S. Inan, and T.F. Bell, Spatial structure of sprites, *Geophys. Res. Lett., 25,* 2123, 1998b.

Rowland, H. L., R. F. Fernsler, J. D. Huba, and P. A. Bernhardt, Lightning driven EMP in the upper atmosphere, *Geophys. Res. Lett., 22,* 361, 1995.

Sentman, D. D., and E. M. Wescott, Red sprites and blue jets: Thunderstorm-excited optical emissions in the stratosphere, mesosphere, and ionosphere, *Phys. Plasmas, 2,* 2514, 1995.

Sentman, D. D., E. M. Wescott, D. L. Osborne, D. L. Hampton, and M. J. Heavner, Preliminary results from the Sprites94 campaign: Red Sprites, *Geophys. Res. Lett., 22,* 1205, 1995.

Taranenko, Y. N., U. S. Inan, and T. F. Bell, Interaction with the lower ionosphere of electromagnetic pulses from lightning: Heating, attachment, and ionization, *Geophys. Res. Lett., 20,* 1539,1993a.

Taranenko, Y. N., U. S. Inan, and T. F. Bell, The interaction with the lower ionosphere of electromagnetic pulses form lightning: Excitation of optical emissions, *Geophys. Res. Lett., 20,* 2675, 1993b.

Wescott, E. M., D. Sentman, D. Osborne, D. Hampton, and M. Heavner, Preliminary results from the Sprites94 aircraft campaign, 2, Blue jets, *Geophys. Res. Lett., 22,* 1209, 1995.

Uman, M.A., *The Lightning Discharge*, Academic, San Diego, Calif., 1987.

U. S. Inan, V. P. Pasko, and G. Veronis, STAR Laboratory, Stanford University, Stanford, CA 94305. (inan@nova.stanford.edu; pasko@nova.stanford.edu; veronis@nova.stanford.edu.)

(Received September 24, 1998; revised January 25, 1999; accepted March 2, 1999.)